Pareto Optimal Spectrally Selective Emitters for Thermophotovoltaics via Weak Absorber Critical Coupling

Nari Jeon[1], Jonathan J. Hernandez[2,4], Daniel Rosenmann[3], Stephen K. Gray[3], Alex B. F. Martinson[1,]*, Jonathan J. Foley IV[4,]*

[1]Materials Science Division, Argonne National Laboratory, Argonne, Illinois, 60439, USA

[2]Union County College, 1033 Springfield Avenue, Cranford, New Jersey, 07016, USA

[3]Nanoscience and Technology Division, Argonne National Laboratory, Argonne, Illinois, 60439, USA

[4]Department of Chemistry, William Paterson University, 300 Pompton Road, Wayne, New Jersey, 07470, USA

ABSTRACT

Tailoring the emission spectra of a thermophotovoltaic emitter away from that of a blackbody has the potential to minimize transmission and thermalization loss in a photovoltaic receiver. Selective thermophotovoltaic emitters could lead to solar energy conversion with efficiency greater than the Shockley-Queisser limit and could facilitate the generation of useful energy from

21   waste heat. We introduce a new design to radically tune thermal emission that leverages the

22   interplay between two resonant phenomena in a simple planar structure – absorption in weakly-

23   absorbing thin films and reflection in multi-layer dielectric stacks. We employ a virtual screening

24   approach based on Pareto optimality to identify a small number of promising structures for a

25   selective thermal emitter from a search space of millions, several of which approach the ideal

26   values of a step-function selective thermal emitter. One of the more simple and optimal of these

27   structures is experimentally fabricated and evaluated, which includes a weakly-absorbing alloy

28   with tailored optical properties fabricated by atomic layer deposition. The versatility of the

29   design and fabrication approach result in an emitter with excellent spectral density (0.8 W/cm^2 sr)

30   and spectral efficiency (46.8%) at 1373 K. Future experimental challenges to a more accurate

31   realization of the optimal structures calculated are also considered, including a weak absorber

32   with more ideal optical constants and even greater thermal stability.

33   **Introduction**

34   The broad range of solar photon energies (0.5 – 4.1 eV) fundamentally limits single gap solar

35   photovoltaics (PV) efficiency, owing largely to photons with energies below the bandgap that do

36   not contribute to photocurrent and photons with energies above the bandgap, which result in

37   losses from a variety of dissipation mechanisms including thermalization.[1-7] The potential benefit

38   of "reshaping" the solar spectrum to minimize these losses in a target PV cell is a central idea

39   behind solar thermophotovoltaics (STPVs).[3, 6, 8] In a STPV device, concentrated sunlight is

40   incident upon an absorber that is in thermal contact with an emitter. The thermal radiation of this

41   hot emitter may be tailored to match the bandgap of a PV cell, see **Figure 1**, which allows for

42   STPVs with a significantly greater fundamental limit (85 %) than traditional single junction PVs

43   (33%).[3] More generally, thermophotovoltaics (TPVs) utilize the same selective emitter paired

44   with a PV cell, but the heat source may come from a variety of non-solar sources, including

45   waste heat generated by engines and reactors. Thus, TPV and STPV devices or, for short, S(TPV)

46   devices, could constitute a versatile clean energy strategy.
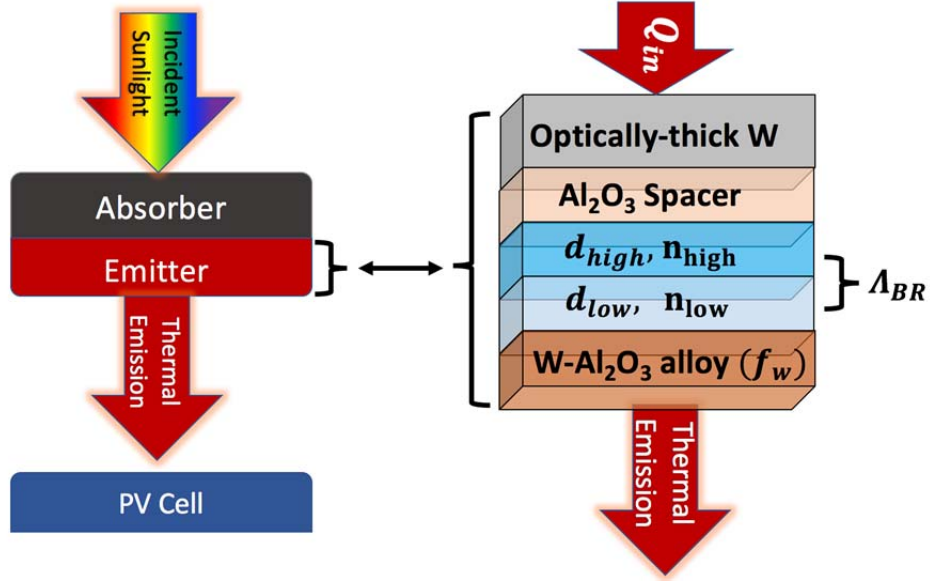
Figure 1 Schematic of a STPV system (left) and representative illustration of the novel emitter design (right). Structural parameters that are varied in our virtual screening approach include the Bragg reflector (BR) dielectric layer thicknesses, d_{high} and d_{low}, of n_{high} and n_{low} refractive indices, the number of such pair layers, Λ_{BR}, and the W volume fraction of the W-Al$_2$O$_3$ alloy, f_W. Heat (Q_{in}) flows from the absorber to the emitter via an optically-thick W layer, and spectrally-tailored thermal emission radiates from the W-Al$_2$O$_3$ side. Here the n_{high} and n_{low} are taken to be characteristic of TiO$_2$ and SiO$_2$, respectively.

However, it remains the case that (S)TPVs are not yet a significant players in the clean energy market. Experimentally-realized efficiencies of STPV devices are currently far below the Shockley-Queisser limit.[3, 9-12] The selective thermal emitter is a critical component for (S)TPV devices which we characterize with two figures-of-merit. The useful power density, P, is the flux of photons emitted with energies at or above the PV's bandgap, $\dot{N}_{\lambda \leq \lambda_{bg}}$, multiplied by the bandgap energy, E_{bg}:

$$P = E_{bg} \cdot \dot{N}_{\lambda \leq \lambda_{bg}} \quad , \tag{1}$$

where the wavelength associated with the bandgap is $\lambda_{bg} = hc/E_{bg}$, with h being Planck's constant and c being the speed of light. The photon flux, in turn, depends on the temperature and spectral properties of the emitter,

$$\dot{N}_{\lambda \leq \lambda_{bg}} = \int_0^{\lambda_{bg}} \frac{\lambda}{hc} \rho(\lambda, T) \, \epsilon(\lambda) \, d\lambda \quad , \tag{2}$$

where $\rho(\lambda, T)$ is the blackbody spectral density and $\epsilon(\lambda)$ is the emissivity spectrum of the emitter. Assuming the emitter structure is at thermal equilibrium, $\epsilon(\lambda)$ is taken to be the absorption spectrum of the emitter (Kirchoff's law).[13] Therefore, the amount of useful power,

3

67   (insofar as a particular PV cell is concerned) generated per unit area of the emitter surface can be

68   rewritten in a manner that permits straightforward computation once the temperature and

69   emissivity are known[14]:

$$P = \int_0^{\lambda_{bg}} \frac{\lambda}{\lambda_{bg}} \rho(\lambda, T)\, \epsilon(\lambda)\, d\lambda. \tag{3}$$

70   The λ/λ_{bg} factor captures the disadvantage of photons with energies greater than the bandgap

71   energy (i.e., $\lambda < \lambda_{bg}$) since these photons will not be as efficiently used as those at exactly the

72   bandgap energy. In this simple view, the spectral conversion efficiency (η_s)[14] of the emitter/PV

73   pair is then given by dividing the useful power density (P) by the total emitted power density,

74   P_{inc}:

$$\eta_s = \frac{P}{P_{inc}} = \frac{\int_0^{\lambda_{bg}} \frac{\lambda}{\lambda_{bg}} \rho(\lambda, T)\, \epsilon(\lambda)\, d\lambda}{\int_0^{\infty} \rho(\lambda, T)\, \epsilon(\lambda)\, d\lambda}. \tag{4}$$

75   Both of these figures of merit play important roles in the overall efficiency of the (S)TPV device.

76   A high η_s is important for minimizing thermalization losses, while a large P is important for

77   minimizing efficiency losses in the PV cell due to loss of open circuit voltage. A more detailed

78   discussion of these considerations can be found in the supporting information, as well as in Ref.

79   [6, 15].

80   The emissivity, $\epsilon(\lambda)$, is a key quantity in determining both η_s and P for a given candidate emitter

81   structure. For example, if $\epsilon(\lambda)$ is a delta function at $\lambda = \lambda_{bg}$, then the emitter has perfect spectral

82   efficiency ($\eta_s = 1$) but low P. Alternatively, if the emissivity has the form of a step function

83   ($\epsilon(\lambda) = 1$ for $\lambda \leq \lambda_{bg}$ and $\epsilon(\lambda) = 0$ otherwise), then P is maximized, although η_s will be less

84   than unity. (A blackbody emitter is one that has $\epsilon(\lambda) = 1$ for all λ, and will have the same P as

85   the step-function case but will have a lower η_s due to a larger P_{inc} - see Eq. 4.) Optimal S(TPV)

86   emitters will have thermal emission profiles between the two ideal limits of a step-function and a

87   delta function.

88   From the above considerations, we see that the design of selective emitters for (S)TPV

89   applications requires achieving large values of two conflicting objectives, the useful power

90   density, P, and the spectral efficiency, η_s. That is, P may increase at the expense of η_s increasing

91   and vice versa. Pareto optimality is a useful concept for considering such competing

92   objectives.[15-18] In this context, a Pareto optimal emitter structure is one with a P value that

93   cannot be increased (by variation of structural parameters) without decreasing η_s and vice versa.
94   There can be many such Pareto optimal structures that form a curve or "Pareto front" in a
95   relevant portion of the η_s-P space. A decision beyond the simple trade-off must then later be
96   made regarding the acceptable magnitudes of the two objectives as to which structure along a
97   Pareto front is best for an application at hand. Pareto analysis has recently been used in other
98   virtual design approaches, including the design of solar absorbers[15] and the design of molecules
99   for efficient organic light emitting diodes[16].

100   A variety of planar and nanostructures have previously been explored in search of high-
101   performance selective emitters, several of which are summarized in **Table 1**.[19] The greatest η_s
102   simulated to date is ~59% from a W photonic crystal (2D square array of cylindrical holes)
103   fabricated via interferometric lithography using a trilayer resist process.[20] Among experimental
104   studies of high temperature emission, the highest reported η_s is ~35% from a HfO_2-coated Ta
105   photonic crystal.[21] A more detailed comparison would also consider steep emittance angles –
106   conditions under which the P and/or η_s performance of many designs quickly declines.
107   Furthermore, the metrics for many of the reported emitters are based on simulations alone or on
108   room temperature reflectance measurements, leaving much room for evaluation of P and η_s at
109   useful operating temperatures (>1200 K). As shown in **Table 1**, we identify simple simulated
110   structures with record η_s while maintaining similar or superior P. Likewise, the structures
111   fabricated herein show record η_s while maintaining a P similar to previous experimental reports.

112   The structures under investigation in this work can be classified as L-layer planar structures with
113   variations only along the $z-$axis and that are isotropic along the $x-$ and $y-$axes, where L is the
114   number of layers. The base layer (in thermal contact with the hypothetical absorber in **Figure 1**)
115   consists of an optically-thick tungsten (W) substrate. This layer is separated from a Bragg
116   reflector (with alternating SiO_2 and TiO_2 layers) by a thin alumina layer that aids adhesion while
117   having negligible impact on the optical properties; we note that the negligible impact of such
118   adhesion layers cannot be universally assumed[22], and we will pursue fabrication strategies to
119   avoid them in the future.

120   The Bragg reflector supports an alloy of tungsten in alumina with optical properties that are
121   tunable with volume fraction.[23] Spectrally-tailored thermal radiation is designed to be emitted
122   from the surface of the thin alloy layer and collected by a InGaAsSb PV cell. The interplay
123   between the Bragg reflector and the alloy layer plays a critical role in defining the emissivity of
124   the structure, and by extension, its η_s and P figures-of-merit. Under certain conditions,
125   absorption resonances in the alloy layer may be critically coupled to the reflection resonances of
126   the Bragg reflector, leading to strong selective thermal emission profiles of the composite

5

127 structure. Similar critical coupling mechanisms have been utilized, for example, to realize
128 extraordinary absorption in graphene monolayers/photonic crystal composites,[24-25] as well as
129 enhanced absorption[26] and Forster Resonance Energy Transfer

	$P_\perp$ [W/cm²sr]	η_s[%]	PV (bandgap)	T [K]	Method
W Photonic crystal[20]	1.9	58.9	InGaAsSb (0.55eV)	1500	Simulation
VO₂ photonic crystal[12]	1.4	40.4	In$_{0.69}$Ga$_{0.31}$As (0.62eV)	1500	Simulation
W graded index[27]	3.0	56.2	GaSb (0.73 ev)	1750	Simulation
This work (theory)	0.6	64.5	InGaAsSb (0.55 eV)	1273	Simulation
This work (theory)	1.7	66.5	InGaAsSb (0.55 eV)	1500	Simulation
This work (theory)	3.3	66.4	InGaAsSb (0.55 eV)	1700	Simulation
Ta photonic crystal[11]	1.8	48.6	InGaAsSb (0.54 eV)	1500	Reflection @ RT
W/HfO₂ multilayer[28]	0.3	44.0	InGaAsSb (0.55 eV)	1273	Reflection @ RT
Ta photonic crystal[21]	0.5	34.5	InGaAs (0.62 eV)	1255	Emission @ 1255 K
Si/SiO₂/Pt photonic crystal[29]	0.1	19.3	InGaAsSb (0.55 eV)	939	Emission @ 939 K
W/HfO₂ multilayer[28]	0.6	33.5	InGaAsSb (0.55 eV)	1273	Emission @ 1273 K
This work (experiment)	0.5	45.4	InGaAsSb (0.55 eV)	1273	Emission @ 1273 K
This work (experiment)	0.8	46.8	InGaAsSb (0.55 eV)	1373	Emission @ 1373 K

130

131 **Table 1.** Calculated and experimental performance of selective emitters considering only normal
132 emission per convention. See Supporting Information Eq. (S6) for the definition of $P_\perp$. The literature
133 values of selective emittance in Table 1 may differ from some reports in which the figure of merit does
134 not explicitly account for the disadvantage of photons with energies greater than the bandgap.

135 (FRET)[30] in thin films composed of J-aggregates critically coupled to a Bragg Reflector. In our
136 design, the conditions for critical coupling between the alloy layer and the Bragg reflector are as
137 follows: the frequency of resonant absorption in the alloy layer is equal to the frequency of
138 resonant reflection in the Bragg reflector, and the absorption rate of the alloy layer is equal to the

139   leakage rate of the Bragg reflector. The resonance frequencies and leakage rates of Bragg

140   reflectors are tuned through geometry and choice of material. Similarly, the absorption frequency

141   and rate in metal-in-dielectric alloys can be tuned through choice of materials and volume

142   fraction of the alloy. The tungsten-alumina alloys simulated here exhibit a weak resonant

143   absorption in the near-IR (~1500 nm), which is ideal for (S)TPV applications.

144   Our virtual screening approach utilizes multi-layer Fresnel theory calculations via the transfer

145   matrix equation[31] to determine the absorbance (and thus emissivity) for $\approx$ 3 million candidate

146   structures. The figures of merit P and η_s when paired with a common low-bandgap PV,

147   InGaAsSb (λ_{bg} = 2254nm, E_{bg}= 0.55 eV) were determined and Pareto optimal points were

148   identified. We further define a metric that quantifies the degree of critical coupling in our

149   structures (Equation 6 below) and show that high degrees of critical coupling are correlated with

150   Pareto optimality. One Pareto optimal structure exhibits excellent computed performance: η_s =

151   66% and $P_\perp$ = 3.3 W/cm^2 sr at 1700K (see SI Eq. S6 for the definition of $P_\perp$). At 1500K the

152   same structure is also predicted to exhibit record η_s, with P also among the highest reported to

153   date (see Table 1). A related Pareto optimal structure with excellent η_s (60%) and even

154   greater $P_\perp$ (3.9 W/cm^2 sr) at 1700K was targeted for experimental fabrication with and without

155   the weak absorber and subsequently characterized at high temperature to identify potential

156   limitations in experimental feasibility and stability. Although the weak absorber fabricated was

157   found to have non-ideal optical properties and limited thermal stability, the performance after

158   accounting for non-idealities in each component layer was found to resemble theoretical

159   predictions. The spectral emissivity of a Pareto optimal structure without alloy at 1373K

160   exhibited record η_s = 46.8% and a respectable $P_\perp$ = 0.8 W/cm^2 sr.

161   **Results**

162   The planar structures computationally screened include optically-thick tungsten only (denoted

163   'W'), variable Bragg reflectors only on an optically-thick tungsten substrate (denoted 'BR + W'),

164   and variable W/Alumina alloys with variable Bragg reflectors on an optically-thick tungsten

165   substrate (denoted 'Alloy + BR + W'), see **Figure 1**. It can be seen in **Figure 2** that in each case,

166   the additional degrees of freedom added by the subsequent structures significantly improves the

167   optimal η_s and P values that are possible. As such, the Pareto front for the entire solution space

168   is found within the 'Alloy + BR + W' structures. One select Pareto optimal structure and an

169   analogous structure without alloy are examined in more detail below (denoted 'Select Alloy +

170   BR + W' and 'Select BR + W').

171
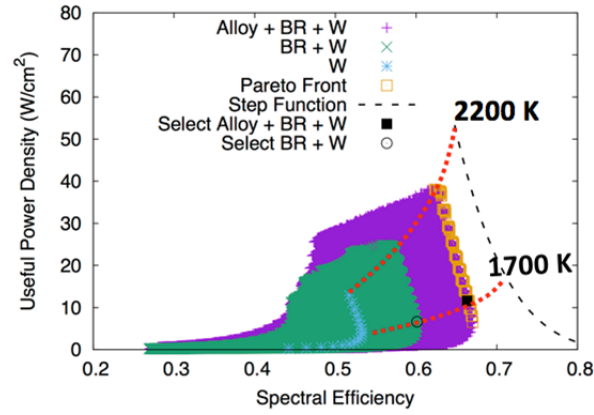
172   **Figure 2.** Comparison of possible values for useful power density and spectral effiency for a variety of
173   planar structures at temperatures between 1200K and 2200K when λ_{BG} = 2254 nm. The orange squares
174   demark the Pareto front. The red-dashed lines intersect solutions at select temperatures (1700 K and 2200
175   K). An idealized emitter with step-function emissivity is also plotted for comparison. The simple Pareto
176   optimal structure (and analogous structure without alloy) selected for further examination has a Λ_{BR} =
177   1.5 Bragg reflector, **Figure 3**.

178

179
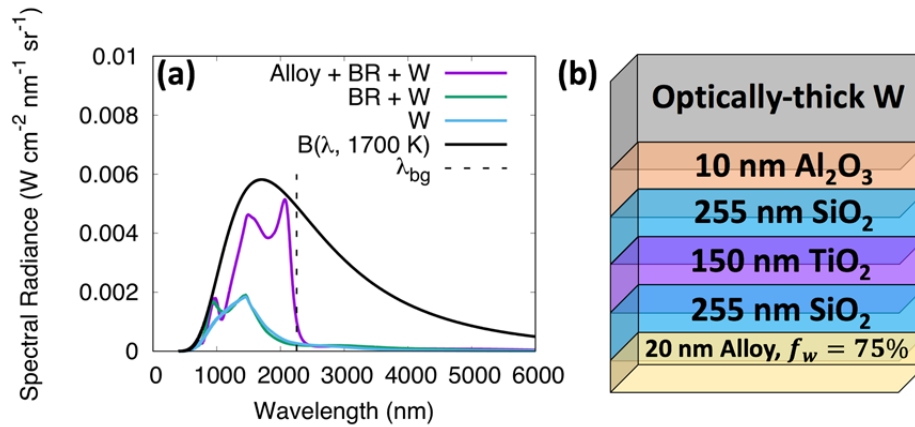
180   **Figure 3.** (a) Theoretical normal thermal emission spectrum of selected Pareto-optimal structure with and
181   without 20-nm thick W-Al$_2$O$_3$ alloy (f_W = 75%) weak absorber, compared to a W-only and blackbody
182   emitter at 1700 K. Alloy + BR + W structure is predicted to have η_s = 66% and
183    $P_\perp$ = 3.3 $W\ cm^{-2}\ sr^{-1}$. A dashed line illustrates the λ_{bg} = 2254 of the hypothetical energy-receiving PV.
184   (b) Schematic of a simple Pareto optimal structure selected for further examination.

185   A tungsten substrate with optical constants from the literature is seen to be an advantageous base

8

186   layer as its emissivity is already weighted heavily below the desired bandgap. The addition of the

187   Bragg reflector in this case has only a minor impact on the short wavelength emissivity.

188   However, as shown in **Figure 4**, some Bragg reflectors alone can strongly shape the emissivity

189   and substantially improve P and η_s compared to bare tungsten. A striking calculated increase in P

190   upon addition of the alloy can be understood from the emission spectra in **Figure 3**, which

191   predicts emission with spectral radiance nearly equal to that of the black body limit ($\epsilon(\lambda) = 1$)

192   just below the PV bandgap. The peak around 1500 nm is also strongly enhanced. The virtual

193   screening algorithm we apply assumes that the emissivity is angle-independent and that the

194   emitted power density decreases as $\cos(\theta)$ where θ is the emission angle with respect to the

195   normal; a more detailed discussion of angular dependence can be found in the Supporting

196   Information. Under the $\cos(\theta)$ assumption for the angular dependence of the thermal emission,

197   the target structure is calculated to exhibit η_s and P of 66 % and 10.6 W/cm^2, respectively at

198   1700K. Explicit inclusion of the angle dependence of the emissivity of the structure (see the

199   supporting information and Eq. S4) yields remarkably similar performance for the structure

200   illustrated in **Figure 3**. This structure is predicted to retain 90% of its spectral selectivity over

201   angles up to 80% (see **Figure S1**) and overall η_s and P of 62 % and 9.1 W/cm^2, respectively at

202   1700K.

203   The experimental feasibility of each component in the Pareto optimal target structure was

204   evaluated in turn. The volume fraction of W in Al_2O_3 was tuned by cycle ratio in an atomic layer

205   deposition (ALD) process and the thickness controlled by the total number of supercycles. The

206   real and imaginary index of each layer was deduced from spectroscopic ellipsometry to be within

207   21 % of the modelled data for oxides and within 13 % for the W substrate. The largest deviation

208   was for W grown by ALD (> 200%, see **Figure S2**), which is known to include a significant

209   fraction of Si and F.[32-33] Furthermore, the real and imaginary index of the variable fraction alloy

210   were found to be more accurately modeled by a Bruggeman approximation[34] than by Maxwell-

211   Garnett theory (see discussion in the Supporting Information). As such, a second computational

212   screening was undertaken that implements the experimentally realized materials properties of

213   this study as inputs. The results, shown in **Figure S3**, suggest that good control of the optical

214   constants in each layer is paramount to achieving the best figures-of-merit. In particular, η_s is

215   most sensitive to increases in the imaginary part of the refractive index at $\lambda_{bg} > 2254$ nm which

216   increase P_{inc} and thereby reduce η_s.

217   Pareto optimal structure with BR + W ($\Lambda_{BR} = 2$) and alloy + BR + W ($\Lambda_{BR} = 1.5$) were chosen

218   for experimental fabrication at operating temperatures > 1000K. After mild densification of the

219   oxide layers, which results in a slight blue-shift of resonances, the reflectance of BR + W and

220 alloy + BR + W samples were observed to remain stable upon annealing at 1273K and 1073K for
221 2hr under an atmosphere of dry Ar (see SI for details).

222 The predicted emission spectra were recalculated with experimentally realized optical constants
223 and thicknesses and compared to experimental emission spectra, **Figure 4**.

224
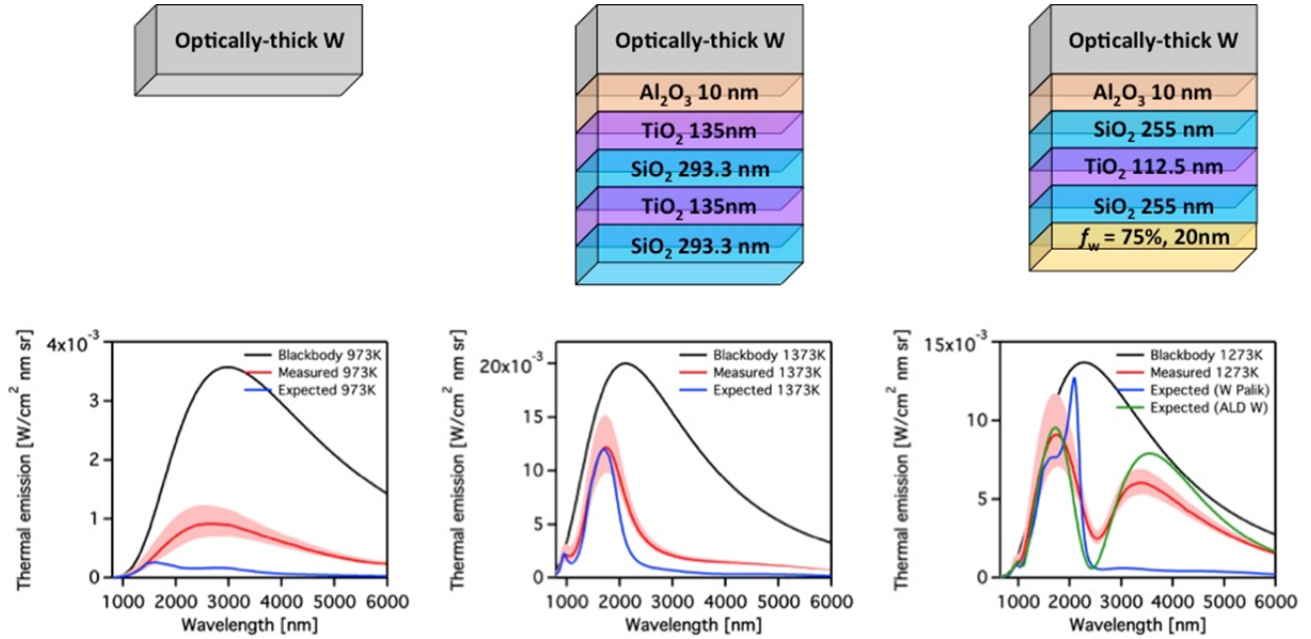
Figure 4. Theoretical and experimental normal thermal emission of W-only at 973K, BR + W at
1373K, and Alloy + BR + W at 1273 K. Red shaded region represent error range assuming that
the actual temperature of the sample surface is within ±50 °C of the nearby thermocouple.

228 Emission of bare polished W substrate at 973 K was measured to be larger than expected, likely
229 due to surface oxidation and roughening as indicated by visual evidence of substrate
230 discoloration and significant loss of specular reflection. Even after implementation of an
231 additional water and oxygen scrubber in the inert gas feed, as well as high temperature carbon
232 felt, the purity of the nominally inert atmosphere of the heating stage could not be sufficiently
233 suppressed to avoid the oxidation of the readily oxidized W surface. In contrast to bare W, the
234 alloy + BR + W and BR + W samples maintained the same color and mirror finish after the same
235 emission measurements to even higher temperature. That the oxide layers of BR protect the W
236 surface from oxidation relaxes the requirements on working atmosphere for stable operation, and
237 provides significant temperature stability advantage over previous reports, which may further
238 utilize dilute H_2 flow.[20] As predicted, the emissions from BR + W and alloy + BR + W approach
239 that of a blackbody for wavelength less than 2254 nm and are dramatically suppressed at longer
240 wavelengths for the case of BR + W. In both cases, the measured useful power densities were
241 slightly greater than predicted while the measured spectral efficiencies were lower. For BR + W,

242   the primary cause of the enhanced thermal emission in the mid IR range > 2000 nm is a change

243   of electron phonon collision frequency at high temperatures, which is not captured in the

244   simulations, leading to higher emissivity and additional undesired emission in this range.[28, 35-36]

245   The emission of alloy + BR + W for wavelength less than 2254 nm is significantly enhanced to

246   that of W-only and very close to predictions. The alloy + BR + W even more strikingly enhances

247   emission at λ_{bg} < 2254 nm; however, the alloy also results in significant emission in λ_{bg} > 2254

248   nm, which reverses any potential improvement in η_s. This discrepancy originates from an

249   imaginary refractive index for ALD-grown W in the alloy that is significantly larger than

250   literature values for pure, bulk W. The η_s and P of the oxidized W at 973 K is 15.6 % and 0.1

251   W/cm^2, BR + W at 1373 K is 46.8 % and 2.4 W/cm^2, and alloy + BR + W at 1273 K is 27.1 %

252   and 1.9 W/cm^2, respectively.

253   From the above analysis, the overall system efficiency for a thermophotovoltaic system that

254   would implement these emitters may be estimated by using either an idealized, or previously

255   benchmarked, InGaAsSb photovoltaic with parameterized values of open circuit voltage (V_{OC})

256   and fill factor (FF) for a given short-circuit current density (J_{SC}),[37] which is calculated by

257   assuming room temperature operation of the cell and 80% external quantum efficiency (EQE).[38]

258   That is, J_{SC} is simply P divided by the voltage corresponding to the useful photons threshold

259   (0.55 V) which is further multiplied by a scalar in the case of the benchmarked device.   **Table 2**

260   summarizes the predicted thermophotovoltaic conversion efficiency of heat to electrical power, η

261   $_{TPV}$, calculated as[38]

$$\eta_{TPV} = \frac{J_{SC}V_{OC}FF}{P_{inc}} \qquad (5)$$

263   for (1) an ideal PV cell and the ideal Pareto optimal emitter calculated here, (2) an ideal PV cell

264   and the emitter measured herein, and (3) a previously benchmarked PV cell[37] and the emitter

265   measured herein. We assumed 100% EQE, 0.55 eV V_{OC}, and 81.6% FF for the ideal PV.[39] If the

266   heat was provided by a perfect solar absorber then η_{TPV} is directly comparable to conventional

267   photovoltaic efficiency. A significant reduction of overall system efficiency (60~70%) is

268   predicted when experimental InGaAsSb PV parameters are used, consistent with literature

269   reports,[9, 29] and points to the need for further improvement in small bandgap PV efficiency.

270

271

272

	Alloy/BR/W at 1273 K	BR/W at 1373 K	(Oxidized) W at 973 K	SiC at 1273 K
Ideal PV + Theoretical Emitter	52.5	49.1	25.3	18.4
Ideal PV + Experimental Emitter	22.1	38.2	12.8	
Benchmarked PV + Ideal Emitter	19.4	18.3	6.8	6.8
Benchmarked PV + Experimental Emitter	8.2	14.0	3.9	

277 **Table 2.** Thermophotovoltaic efficiency, η_{TPV} (%) projected for (1) an ideal InGaAsSb PV and an optimal
278 theoretically-calculated emitter, (2) an ideal PV and the experimentally-measured emitter, and (3) a
279 previously benchmarked PV cell and the experimentally-measured emitter.
280
281 In the most conservative case (3), the η_{TPV} projected for our experimental BR + W emitter
282 working at 1373K in a TPV system is 14.0 %. Note that the efficiency for the benchmarked PV
283 is not equal in each case because FF and V_{OC} vary with J_{SC}.[37] The η_{TPV} with either BR + W or
284 alloy + BR + W realized emitter is projected to be greater than that of the InGaAsSb PV alone
285 under standard AM1.5 spectra (~6.3%),[3] signifying that the TPV is improving solar conversion
286 efficiency. However, a more ideal selective emitter or more ideal PV are required to exceed the
287 efficiency of traditional single junction PV (28.8 %).[40] The calculated efficiency, projected from
288 the experimentally realized emitter, is also slightly greater than that of the most efficient
289 experimental system reported to date (~10.2%).[3] The weak-absorber approach implemented
290 herein is also simpler, as it does not include a cool-side selective optical filter on the PV, as in
291 previous reports.[3] The enhanced η_{TPV} calculated from experimental emission herein originates
292 largely from the spectral selectivity of the BR and the stabilization of selective emittance at high
293 temperature. Projected η_{TPV} values may be further improved by 1) better leveraging the critical
294 coupling approach through improvement of experimental material optical properties and 2)

295 increasing the stable operational temperature of the emitter through the use of more temperature-
296 tolerant materials and combinations.

297 As a central hypothesis driving this overall structure design is the critical coupling of the Bragg
298 reflector and thin-film alloy, we define a metric that quantifies the degree of critical coupling
299 (D_{CC}). The condition for critical coupling is that the absorption resonance frequency and
300 bandwidth of the thin-film alloy layer should match the resonance frequency and bandwidth
301 associated with the *stored energy* spectrum of the Bragg reflector,[25] which can be derived from
302 the transfer matrix equations (see Supporting Information). A natural way to define the degree
303 of critical coupling is therefore to compute the overlap of the absorption spectrum of the alloy
304 ($A_{Alloy}(\lambda)$) with the stored energy spectrum of the Bragg reflector ($E_S(\lambda)$),

305
$$D_{CC} = \frac{\int_{\lambda_{min}}^{\lambda_{max}} A_{Alloy}(\lambda)\, E_S(\lambda)\, d\lambda}{\left(\int_{\lambda_{min}}^{\lambda_{max}} A_{Alloy}(\lambda)\, A_{alloy}(\lambda)\, d\lambda\right)^{\frac{1}{2}} \left(\int_{\lambda_{min}}^{\lambda_{max}} E_S(\lambda)\, E_S(\lambda)\, d\lambda\right)^{\frac{1}{2}}}. \tag{6}$$

306

307 That a high degree of critical coupling is characteristic of a Pareto optimal solution in this study
308 can be seen in **Figure 5**. The optimal solutions all exhibit a relatively high degree of critical
309 coupling with values near 0.7 and 0.9. However, interestingly, the highest degrees of critical
310 coupling are not associated with simultaneously high η_s and P as seen by only non-optimal
311 solutions with $D_{CC} > 0.9$.

312
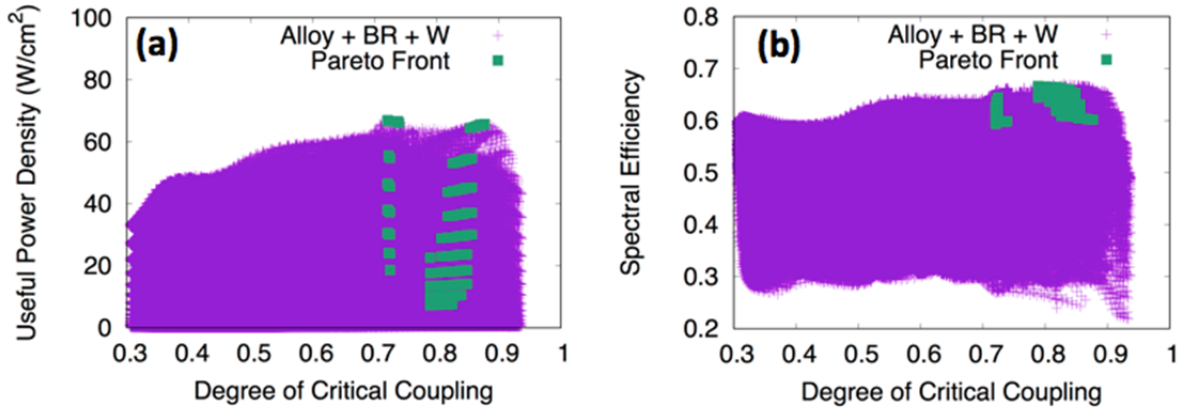
314 **Figure 5.** Comparison of possible values for P and η_s plotted against degree of critical coupling for
315 emitters at temperatures between 1200 K and 2200 K when $\lambda_{BG} = 2254$ nm.

316
317
318

319 **Conclusions**
320 We showed how ideas of Pareto optimality and critical coupling provide a clear path to
321 significantly higher performing thermophotovoltaic emitters. We identify a route to tunable
322 emission with exceptionally simple planar stacks based on less than six layers. This approach
323 provides contrast to recent trends toward more complex nanostructured selective emitters,
324 although it may not be incompatible with it. Experimental validation of one optimal solution
325 results in a good match to the predicted selective emission structure after accounting for
326 experimental non-idealities, most notably a weak absorber alloy layer with non-ideal optical
327 properties. Additional development of more thermally stable oxides and more tunable and
328 temperature stable weakly absorbing alloys are expected to further increase the experimentally
329 achievable emitter figures-of-merit and, thereby, themophotovoltaic system efficiency.

330

331 **Methods**

332 **Computational Methods**

333 The emissivity of the structure is equated to the absorbance (Kirchoff's law) and is calculated
334 from

$$\epsilon(\lambda) = 1 - R(\lambda) - T(\lambda) \qquad (7)$$

335 where $R(\lambda)$ and $T(\lambda)$ are the reflection and transmission of light at wavelength λ incident from
336 the alloy side. Because of the 1D nature of the structures, these quantities can be calculated
337 analytically by solving Fresnel's equations via the transfer matrix approach[31] (see Supporting
338 Information). These calculations take as input the thickness and wavelength- dependent (and
339 sometimes complex) refractive index of each layer, as well as the wavelength, polarization, and
340 angle of incidence of light.

341 Our computational search for high performance emitter structures varies the following structural
342 parameters: (1) the volume fraction of tungsten in the tungsten-alumina alloy (f_W), (2) the
343 number of dielectric pair layers (or periods) in the Bragg reflector (Λ_{BR}), (3) the thickness of the
344 low refractive index layer in the Bragg reflector (d_{low}), (4) the thickness of the high refractive
345 index layer in the Bragg reflector (d_{high}). The materials that compose the Bragg reflector are
346 chosen to be SiO_2 (low refractive index layer, $n_{low} = 1.45$ in calculations leading to Figure 2 and
347 3) and TiO_2 (high refractive index layer, $n_{high} = 2.1$ in calculations leading to Figure 2 and 3).
348 The alloy layer and alumina spacer layer have their thicknesses fixed at 20 nm and 10 nm for all
349 virtual screening calculations. Several thicker alloy layers were considered for comparison to

350   fabricated structures (e.g. 32 nm, as in Figure 4). We model the alloy layer using an effective

351   medium theory, which maintains the isotropy of this layer in the $x - y$ plane. In this approach,

352   the alloy is considered to consist of uniformly distributed spherical inclusions of tungsten metal

353   embedded in aluminum oxide, based on a previous report of W-Al$_2$O$_3$ alloys prepared by ALD.[23]

354   Maxwell Garnett theory and Bruggeman's approximation[34, 41] are employed to compute the

355   wavelength-dependent refractive index of the alloy (see Supporting Information). In these

356   models, one simply specifies the refractive index of the materials in the alloy along with their

357   volume fractions to arrive at a single dielectric function for the alloy; further details on the

358   refractive indices of the alloy components are described in the Supporting Information. We find

359   that Bruggeman's approximation shows better agreement with alloys generated by ALD at low

360   to moderate volume fractions of tungsten in alumina.

361   The preceding structural parameters are sufficient inputs to solve the Transfer Matrix Equations

362   and compute the emissivity via Eq. (7). The emissivity can therefore be seen to be a function of

363   these four variables, in addition to frequency: $\epsilon(\omega, v_F, d_{low}, d_{high}, \Lambda_{BR})$. From Eqs. (3) and (4),

364   temperature and λ_{BG} are also important parameters for determining the ultimate figures of merit

365   for the emitter.   Consequently, we can see that the spectral efficiency and useful power density

366   are functions of the structural parameters, the band gap, and the temperature. The search space of

367   each parameter λ_{BG} is discretized into 18 equally spaced values. We search values of the volume

368   fraction f_W between 0 and 0.85, values of d_{low} between 180 nm and 435 nm, values of d_{high}

369   between 120 nm and 290 nm, values of Λ_{BR} between 0 and 8.5 (in units of 0.5), and values of T

370   between 1200 and 2200 K. We consider λ_{BG} to be 2254 nm corresponding to InGaAsSb PV cells.

371   We apply a virtual screening approach based on identifying the set of Pareto optimal solutions

372   with respect to the P and η_s figures-of-merit, where a Pareto optimal solution is one that is not

373   dominated by any other solutions in the search space. For the bi-objective search considered in

374   this work, a solution x_i is dominated by the solution x_j if $\eta_s(x_j) \geq \eta_s(x_i)$ and $P(x_j) \geq$

375    $P(x_i)$, along with $\eta_s(x_j) > \eta_s(x_i)$ and/or $P(x_j) > P(x_i)$. Put in simpler terms, no solutions exist

376   in the search space that simultaneously have higher η_s and P values than the Pareto optimal

377   solutions. The set of Pareto optimal solutions is the Pareto front.

378   Once screened for Pareto optimality, structures can be further analyzed for practical features like

379   ease of fabrication. For example, the Pareto front may contain some structures with a very high

380   number of layers in the Bragg reflector, and others with a low number of layers. The structure

381   with a low number of layers would be preferred.

382

383

Experimental Methods

Polished tungsten substrates (1 cm^2) were sourced from MTI Corporation. The dielectric Bragg reflector was deposited by plasma enhanced atomic layer deposition in a commercial ALD system (Fiji, Cambridge NanoTech Inc.). Aluminum oxide (Al$_2$O$_3$) and W were alloyed by ALD in a tube-style viscous flow reactor similar to those previously reported[23] with a processes adapted from literature.[23] The composition could be tuned over a wide range of values by tuning the ALD cycle ratio at constant temperature. Ex-situ annealing was performed in a high temperature tube furnace (MTI GSL-1700X) under 200 SCCM Ar flow using a bubbler filled with mineral oil. The Ar flow was further purified just prior to entering the furnace with an in-line inert gas scrubber (Entegris CE70KFI4R). Samples were further placed on top of a carbon felt pad, which acts as an oxygen getter at high temperature, in an alumina boat. Although samples with oxide Bragg reflectors are relatively insensitive to the purity of the inert gas atmosphere, bare polished W is exceedingly sensitive.

A Nicolet 6700 FTIR spectrometer with external beam port was used to spectrally resolve the thermal emission of samples heated in a controlled-atmosphere Linkam stage (TS1500). In order to determine the power density in absolute units (W cm^{-2} nm^{-1} sr^{-1}) the spectrometer was calibrated with a SiC wafer with format similar to the W substrates. SiC exhibits a thermal emission spectrum with a stable and constant emissivity of ~0.8 over nearly the entire range relevant wavelengths. SiC is also exceptionally resistant to oxidation at high temperatures unlike other commonly used greybody materials such as graphite. The transmittance of the SiC substrate (0.33 mm thickness and one-side polished 4H SiC, MTI corporation) was 3.5 % at 1 μm and decreased rapidly to ~0% for longer wavelengths (see **Figure S7**) eliminating the possibility of significant contribution from the underlying Al$_2$O$_3$ heater cup. The 7 mm diameter and 3 mm deep sample cup was resistively heated by a nearby Pt coil at a rate of 100 °C/min under Ar supply of 60 SCCM. In order to limit the contribution of thermal emission from the heating cup walls (not covered by the substrate) as well as limit the emission angle of acceptance, a 1/8 inch diameter aperture was fixed above the heating stage. The sample emission was reflected by a 90° off-axis paraboloid, before being directed to the external beam port of the FTIR. A sapphire window and CaF$_2$ windows were used for the heating stage and the external beam port of FTIR spectrometer, respectively.

Reflectance spectra of samples were measured via UV-vis-NIR spectrophotometer (Cary 5000) and Nicolet 6700 FTIR with integrating sphere (Mid-IR IntegratIR™).

416

ASSOCIATED CONTENT

Supporting Information.

Detailed derivation of all calculated values, target and actual emitter parameters, target and

actual optical constants, and reflectance spectra are available free of charge.

AUTHOR INFORMATION

Corresponding Authors

*Jonathan J. Foley IV (foleyj10@wpunj.edu)

*Alex B. F. Martinson (martinson@anl.gov)

Author Contributions

SKG, ABFM, and JJF conceived of the project. JJF implemented and executed the virtual

screening methodology; validation and preliminary calculations were performed by JJF and JH.

SKG, ABFM, NJ, and JJF analyzed all computational results. Fabrication and characterization

of emitter structures was performed by NJ and ABFM. The manuscript was written by NJ, SKG,

ABFM, and JJF. All authors have given approval to the final version of the manuscript.
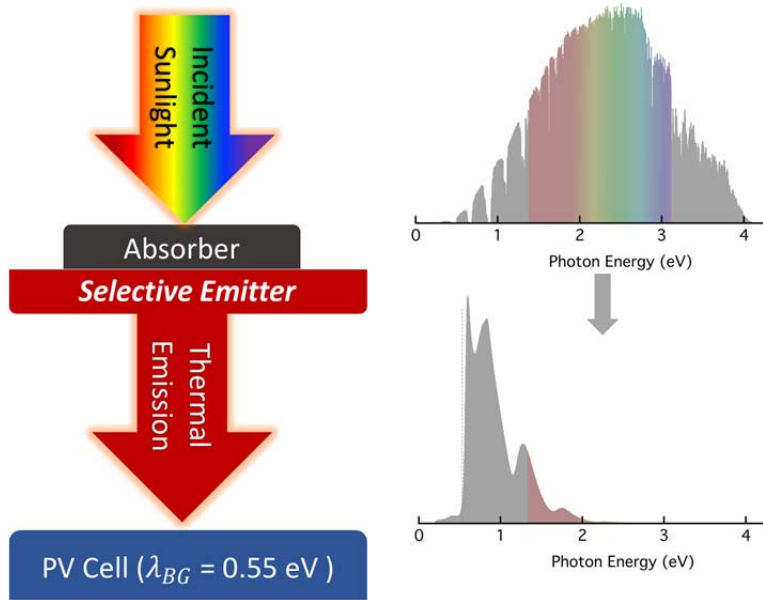
17

445

446   REFERENCES

447   1.   Shockley, W.; Queisser, H. J., Detailed Balance Limit of Efficiency of p-n Junction Solar
448   Cells. *Journal of Applied Physics* **1961**, *32* (3), 510-519.
449   2.   Song, M.; Yu, H.; Hu, C.; Pu, M.; Zhang, Z.; Luo, J.; Luo, X., Conversion of broadband
450   energy to narrowband emission through double-sided metamaterials. *Opt. Express* **2013**, *21* (26),
451   32207-32216.
452   3.   Bierman, D. M.; Lenert, A.; Chan, W. R.; Bhatia, B.; Celanović, I.; Soljačić, M.; Wang,
453   E. N., Enhanced photovoltaic energy conversion using thermally based spectral shaping. *Nature*
454   *Energy* **2016,** *1*, 16068.
455   4.   Datas, A.; Chubb, D. L.; Veeraragavan, A., Steady state analysis of a storage integrated
456   solar thermophotovoltaic (SISTPV) system. *Solar Energy* **2013,** *96*, 33-45.
457   5.   St-Gelais, R.; Zhu, L.; Fan, S.; Lipson, M., Near-field radiative heat transfer between
458   parallel structures in the deep subwavelength regime. *Nat Nano* **2016,** *11* (6), 515-519.
459   6.   Zhou, Z.; Sakr, E.; Sun, Y.; Bermel, P., Solar thermophotovoltaics: reshaping the solar
460   spectrum. *Nanophotonics* **2016,** *5* (1), 1.
461   7.   Badescu, V., Upper bounds for solar thermophotovoltaic efficiency. *Renewable Energy*
462   **2005,** *30* (2), 211-225.
463   8.   Inoue, T.; De Zoysa, M.; Asano, T.; Noda, S., Realization of narrowband thermal
464   emission with optical nanostructures. *Optica* **2015,** *2* (1), 27-35.
465   9.   Ungaro, C.; Gray, S. K.; Gupta, M. C., Solar thermophotovoltaic system using
466   nanostructures. *Opt. Express* **2015,** *23* (19), A1149-A1156.
467   10.   Lenert, A.; Bierman, D. M.; Nam, Y.; Chan, W. R.; Celanovic, I.; Soljacic, M.; Wang, E.
468   N., A nanophotonic solar thermophotovoltaic device. *Nat Nano* **2014,** *9* (2), 126-130.
469   11.   Rinnerbauer, V.; Lenert, A.; Bierman, D. M.; Yeng, Y. X.; Chan, W. R.; Geil, R. D.;
470   Senkevich, J. J.; Joannopoulos, J. D.; Wang, E. N.; Soljačić, M.; Celanovic, I., Metallic Photonic
471   Crystal Absorber-Emitter for Efficient Spectral Control in High-Temperature Solar
472   Thermophotovoltaics. *Advanced Energy Materials* **2014,** *4* (12), 1400334-n/a.
473   12.   Ye, H.; Wang, H.; Cai, Q., Two-dimensional VO2 photonic crystal selective emitter.
474   *Journal of Quantitative Spectroscopy and Radiative Transfer* **2015,** *158*, 119-126.

475   13.   Rybicki, G. B.; Lightman, A. P., *Radiative Processes in Astrophysics*. Wiley: 2008.

476   14.   Foley, J. J.; Ungaro, C.; Sun, K.; Gupta, M. C.; Gray, S. K., Design of emitter structures
477 based on resonant perfect absorption for thermophotovoltaic applications. *Opt. Express* **2015,** *23*
478 (24), A1373-A1387.

479   15.   Mayer, A.; Gaouyat, L.; Nicolay, D.; Carletti, T.; Deparis, O., Multi-objective genetic
480 algorithm for the optimization of a flat-plate solar thermal collector. *Opt. Express* **2014,** *22* (S6),
481 A1641-A1649.

482   16.   Gomez-Bombarelli, R.; Aguilera-Iparraguirre, J.; Hirzel, T. D.; Duvenaud, D.;
483 Maclaurin, D.; Blood-Forsythe, M. A.; Chae, H. S.; Einzinger, M.; Ha, D.-G.; Wu, T.;
484 Markopoulos, G.; Jeon, S.; Kang, H.; Miyazaki, H.; Numata, M.; Kim, S.; Huang, W.; Hong, S.
485 I.; Baldo, M.; Adams, R. P.; Aspuru-Guzik, A., Design of efficient molecular organic light-
486 emitting diodes by a high-throughput virtual screening and experimental approach. *Nat Mater*
487 **2016,** *15* (10), 1120-1127.

488   17.   Haupt, R. L.; Werner, D. H., *Genetic Algorithms in Electromagnetics*. Wiley: 2007.

489   18.   Ghosh, A.; Tsutsui, S., *Advances in Evolutionary Computing: Theory and Applications*.
490 Springer Berlin Heidelberg: 2012.

491   19.   In some cases, the ηs in Table 1 differs from that reported in the associated publication
492 due to the different way in which spectral efficiency may be calculated, sometimes without the
493 penalty for photons with energy greater than the bandgap.

494   20.   Yeng, Y. X.; Ghebrebrhan, M.; Bermel, P.; Chan, W. R.; Joannopoulos, J. D.; Soljačić,
495 M.; Celanovic, I., Enabling high-temperature nanophotonics for energy applications.
496 *Proceedings of the National Academy of Sciences* **2012,** *109* (7), 2280-2285.

497   21.   Rinnerbauer, V.; Yeng, Y. X.; Chan, W. R.; Senkevich, J. J.; Joannopoulos, J. D.;
498 Soljačić, M.; Celanovic, I., High-temperature stability and selective thermal emission of
499 polycrystalline tantalum photonic crystals. *Opt. Express* **2013,** *21* (9), 11482-11491.

500   22.   Zhou, X.; Jankowska, J.; Li, L.; Giri, A.; Hopkins, P. E.; Prezhdo, O. V., Strong
501 Influence of Ti Adhesion Layer on Electron–Phonon Relaxation in Thin Gold Films: Ab Initio
502 Nonadiabatic Molecular Dynamics. *ACS Applied Materials & Interfaces* **2017,** *9* (49), 43343-
503 43351.

504   23.   Mane, A. U.; Elam, J. W., Atomic Layer Deposition of W:Al2O3 Nanocomposite Films
505 with Tunable Resistivity. *Chemical Vapor Deposition* **2013,** *19* (4-6), 186-193.

506   24.   Piper, J. R.; Liu, V.; Fan, S., Total absorption by degenerate critical coupling. *Applied*
507 *Physics Letters* **2014,** *104* (25), 251110.

508   25.   Piper, J. R.; Fan, S., Total Absorption in a Graphene Monolayer in the Optical Regime by
509 Critical Coupling with a Photonic Crystal Guided Resonance. *ACS Photonics* **2014,** *1* (4), 347-
510 353.

511   26.   Tischler, J. R.; Bradley, M. S.; Bulović, V., Critically coupled resonators in vertical
512 geometry using a planar mirror and a 5 nm thick absorbing film. *Opt. Lett.* **2006,** *31* (13), 2045-
513 2047.

514   27.   Ungaro, C.; Gray, S. K.; Gupta, M. C., Graded-index structures for high-efficiency solar
515 thermophotovoltaic emitting surfaces. *Opt. Lett.* **2014,** *39* (18), 5259-5262.

516   28.   Dyachenko, P. N.; Molesky, S.; Petrov, A. Y.; Störmer, M.; Krekeler, T.; Lang, S.; Ritter,
517 M.; Jacob, Z.; Eich, M., Controlling thermal emission with refractory epsilon-near-zero
518 metamaterials via topological transitions. *Nature Communications* **2016,** *7*, 11809.

29.   Garín, M.; Hernández, D.; Trifonov, T.; Alcubilla, R., Three-dimensional metallo-dielectric selective thermal emitters with high-temperature stability for thermophotovoltaic applications. *Solar Energy Materials and Solar Cells* **2015,** *134*, 22-28.

30.   Akselrod, G. M.; Walker, B. J.; Tisdale, W. A.; Bawendi, M. G.; Bulovic, V., Twenty-Fold Enhancement of Molecular Fluorescence by Coupling to a J-Aggregate Critically Coupled Resonator. *ACS Nano* **2012,** *6* (1), 467-471.

31.   Yeh, P., *Optical Waves in Layered Media*. Wiley: 2005.

32.   Fabreguette, F. H.; Sechrist, Z. A.; Elam, J. W.; George, S. M., Quartz crystal microbalance study of tungsten atomic layer deposition using WF6 and Si2H6. *Thin Solid Films* **2005,** *488* (1), 103-110.

33.   Kima, S.-H.; Kwaka, N.; Kima, J.; Sohn, H., A Comparative Study of the Atomic-Layer-Deposited Tungsten Thin Films as Nucleation Layers for W-Plug Deposition. *J. Electrochem. Soc.* **2006,** *153* (10), G887-G893.

34.   Zhuromskyy, O., *Applicability of Effective Medium Approximations to Modelling of Mesocrystal Optical Properties*. 2016; Vol. 7, p 1.

35.   Ujihara, K., Reflectivity of Metals at High Temperatures. *Journal of Applied Physics* **1972,** *43* (5), 2376-2383.

36.   Winsemius, P.; Kampen, F. F. v.; Lengkeek, H. P.; Went, C. G. v., Temperature dependence of the optical properties of Au, Ag and Cu. *Journal of Physics F: Metal Physics* **1976,** *6* (8), 1583.

37.   Chan, W.; Huang, R.; Wang, C.; Kassakian, J.; Joannopoulos, J.; Celanovic, I., Modeling low-bandgap thermophotovoltaic diodes for high-efficiency portable power generators. *Solar Energy Materials and Solar Cells* **2010,** *94* (3), 509-514.

38.   Qiu, K.; Hayden, A. C. S.; Mauk, M. G.; Sulima, O. V., Generation of electricity using InGaAsSb and GaSb TPV cells in combustion-driven radiant sources. *Solar Energy Materials and Solar Cells* **2006,** *90* (1), 68-81.

39.   Green, M. A., Solar cell fill factors: General graph and empirical expressions. *Solid-state electronics 24* (8), 788-789.

40.   Green, M. A.; Emery, K.; Hishikawa, Y.; Warta, W.; Dunlop, E. D., Solar cell efficiency tables (version 48). *Progress in Photovoltaics: Research and Applications* **2016,** *24* (7), 905-913.

41.   Bohren, C. F.; Clothiaux, E. E.; Huffman, D. R., *Absorption and Scattering of Light by Small Particles*. Wiley-VCH: 2009.

TOC Graphic

554

555